

# Lightning-based propagation of convective rain fields

S. Dietrich, D. Casella, F. Di Paola, M. Formenton, A. Mugnai, and P. Sanò

Institute of Atmospheric Sciences and Climate, Italian National Research Council, Rome, Italy

Received: 3 September 2010 – Revised: 28 January 2011 – Accepted: 23 February 2011 – Published: 27 May 2011

**Abstract.** This paper describes a new multi-sensor approach for continuously monitoring convective rain cells. It exploits lightning data from surface networks to propagate rain fields estimated from multi-frequency brightness temperature measurements taken by the AMSU/MHS microwave radiometers onboard NOAA/EUMETSAT low Earth orbiting operational satellites. Specifically, the method allows inferring the development (movement, morphology and intensity) of convective rain cells from the spatial and temporal distribution of lightning strokes following any observation by a satellite-borne microwave radiometer. Obviously, this is particularly attractive for real-time operational purposes, due to the sporadic nature of the low Earth orbiting satellite measurements and the continuous availability of ground-based lightning measurements – as is the case in most of the Mediterranean region. A preliminary assessment of the lightning-based rainfall propagation algorithm has been successfully made by using two pairs of consecutive AMSU observations, in conjunction with lightning measurements from the ZEUS network, for two convective events. Specifically, we show that the evolving rain fields, which are estimated by applying the algorithm to the satellite-based rainfall estimates for the first AMSU overpass, show an overall agreement with the satellite-based rainfall estimates for the second AMSU overpass.

## 1 Introduction

Since the launch of the first Special Sensor Microwave/Imager (SSM/I) radiometer in 1987 – and especially after the launch of the Tropical Rainfall Measuring Mission (TRMM) space observatory in 1997 – passive microwave (MW) radiometry has been widely and successfully

used to measure precipitation from space. Notably, in order to achieve a spatial resolution that is consistent with the horizontal variability of the geophysical parameters of interest (like precipitation), MW radiometers have been flown, so far, on Low Earth Orbiting (LEO) satellites. This, however, generates coarse temporal sampling since a satellite-borne MW radiometer usually produces, at middle latitudes, only two snapshots per day for any given location over the Earth.

Several MW radiometers are presently operational on LEO satellites – three SSM/I's and one Special Sensor Microwave Imager Sounder (SSMIS) onboard four sun-synchronous near-polar-orbiting satellites of the US Defense Meteorological Satellite Programme (DMSP) (F15, F16, F17 and F18 have ascending equatorial crossing times, ECT's, at 19:37, 20:04, 17:31 and 08:00 LST, respectively); two Advanced Microwave Sounding Units – A and B (AMSU-A, AMSU-B) couples and two AMSU-A/Microwave Humidity Sounder (MHS) couples onboard four sun-synchronous near-polar-orbiting NOAA operational satellites (NOAA-15, -16, -18 and -19, having ECT's at 16:38, 18:49, 13:59 and 13:38 LST, respectively); one AMSU-A/MHS couple onboard the first Meteorological Operational (MetOp-1) satellite of the European EUMETSAT Polar System (EPS), having ECT at 21:31 LST; one AMSU-A/Humidity Sounder for Brazil (HSB) couple and the Advanced Microwave Scanning Radiometer (AMSR-E) onboard the sun-synchronous near-polar-orbiting NASA AQUA satellite, having ECT at 01:30 LST; and finally, the TRMM Microwave Imager (TMI) onboard the equatorial TRMM satellite. Nevertheless, it is evident that because of the sporadic nature of MW observations from LEO satellites, fast evolving processes (such as convective precipitation) can not be adequately monitored using these measurements only.

The situation will certainly improve with the launch of the future Global Precipitation Measurement (GPM) mission (see <http://gpm.gsfc.nasa.gov>; see also Smith et al., 2007) which is presently scheduled for 2013, since the GPM constellation of LEO satellites carrying MW radiometers will



Correspondence to: F. Di Paola  
(francesco.dipaola@artov.isac.cnr.it)

ensure a 3-h temporal sampling over the World. Yet, even that sampling frequency will be scanty for monitoring and nowcasting fast evolving precipitating systems – such as those that are responsible for flash floods in Mediterranean countries (see Llasat et al., 2010). Following the sensitivity study of Gasiewski (1992) on the potential of millimeter-submillimeter frequencies for precipitation retrieval from space, preliminary attempts have been made to evaluate the scientific/technological prospect of sub-hourly rainfall observations from space using submillimeter MW radiometers onboard geostationary (GEO) satellites (e.g., Bizzarri et al., 2007; Di Paola and Dietrich, 2008). Nevertheless, we must emphasize here that while some national and international space agencies have seriously considered this option, for example, the studies that have been carried out by Bizzarri et al. (2005) and Mugnai and Pinori (2005) for the European Space Agency EUMETSAT, the launch of a GEO satellite carrying a MW radiometer can not be foreseen for the present decade.

In the last two decades, various attempts have been made to tackle the MW sampling problem by combining the MW observations of precipitation from LEO satellites with much more frequent, (yet indirect as compared to MW), infrared (IR) observations from GEO satellites. While some MW-IR combined techniques focus on 3-h or longer time scales (e.g., Adler et al., 1994; Huffman et al., 2007), other techniques aim at precipitation estimation on the GEO time scale (every 15/30 min) – e.g., the Naval Research Laboratory (NRL) blended technique (Turk et al., 2000; Turk and Mehta, 2007; Torricella et al., 2007), the University of Birmingham technique (Kidd et al., 2003, 2007), and the Climate Prediction Center (CPC) morphing technique (CMORPH – see Joyce et al., 2004, 2007; see also Kubota et al., 2007). It must be noted that international validation activities have shown that CMORPH often produces more reliable precipitation estimates than other operational satellite algorithms (Ebert et al., 2007). In the morphing approach to satellite-based precipitation mapping, the estimates derived from the upwelling multi-frequency MW brightness temperature ( $T_B$ ) measurements are propagated by motion vectors derived from GEO IR data. Again, it is important to take into account that CMORPH is not a precipitation estimation technique, but rather a technique that creates spatially and temporally complete information using existing precipitation products, like those derived from MW observations. Unfortunately, CMORPH needs two MW-estimated rain fields to generate the in-between rain fields, and obviously this circumstance absolutely does not allow the usage of that tool for real-time applications.

Lightning measurements from ground-based networks may provide useful information for real-time monitoring and nowcasting of convective cloud systems. Indeed they are good proxies to identify location and intensity of convective cells and are continuously and promptly available with a high time rate (usually, every few minutes), for example, Betz et

al. (2008); Bonelli and Marcacci (2008). On the other hand, the problem of using lightning data for quantitative precipitation estimation is still an unresolved one, since the relationships between rainfall and lightning occurrence appear to be highly ambiguous and variable due to the complex nature of the electrification/precipitation processes, for example, Piepgrass and Krider (1982); Sheridan et al. (1997); Tapia et al. (1998); Soula et al. (1998); Petersen and Rutledge (1998); Rivas Soriano et al. (2001); Adamo et al. (2007, 2009).

In this paper, we describe a new morphing technique – which we call Lightning-based Precipitation Evolving Technique (L-PET) – that employs lightning data to propagate forward in time the rain fields estimated from the last available MW observations from space. In addition, a preliminary assessment of L-PET is carried out by using two consecutive AMSU observations (at 13:00 and 15:55 UTC) in conjunction with lightning measurements from the National Observatory of Athens ZEUS detection system (Kotroni and Lagouvardos, 2008), for a scattered convection event that occurred over the island of Sicily, in southern Italy, on 10 October 2009 and for a convective storm occurred over central Europe, on 7 July 2009.

## 2 The MW algorithm for instantaneous rainfall retrieval from space

Since our goal was to develop a technique for real-time monitoring of convective precipitation events, we have considered only the MW radiometers onboard operational satellites – i.e., the cross-track scanning AMSU-A and AMSU-B/MHS couples onboard five NOAA/EUMETSAT sun-synchronous near-polar-orbiting operational satellites. While a detailed description of these radiometers can be found in Kramer (2002), we wish to give here some essential information that is useful for the reader.

These cross-track scanning AMSU-A and AMSU-B/MHS MW radiometers provide images with constant angular sampling across tracks, that implies that the Instantaneous Field Of View (IFOV) elongates as the beam moves from nadir toward the edge of the scan. The elongation is such that for AMSU-A the IFOV is approximately  $48 \times 48 \text{ km}^2$  at nadir and  $80 \times 150 \text{ km}^2$  at the edge of the 2250 km swath, while for AMSU-B and MHS it is approximately  $16 \times 16 \text{ km}^2$  at nadir and  $27 \times 50 \text{ km}^2$  at the edge. For each radiometer, the spatial resolution is constant at all frequencies – 48 km at nadir for AMSU-A and 16 km at nadir for AMSU-B/MHS. AMSU-A was originally intended for atmospheric temperature profiling and, therefore, most frequencies lie in the 54 GHz  $\text{O}_2$  band. On the other hand, AMSU-B or MHS were intended for humidity profiling and, therefore, most frequencies lie in the 183 GHz  $\text{H}_2\text{O}$  band. In the presence of precipitating clouds, the temperature/humidity profiling mission fails and precipitation is observed instead. Since channels are in absorption bands, the observation is particularly valuable over

land because the effects of the highly variable land emissivity are largely damped. The drawbacks with respect to conically scanning radiometers (such as, SSM/I-SSMIS, AMSR and TMI) are the changing pixel size and incidence angle across the swath (implying changing effect of polarization) and the coarse resolution of AMSU-A.

We adopt the AMSU precipitation retrieval algorithm that was developed by Surussavadee and Staelin (2008a) at the Massachusetts Institute of Technology (MIT). This algorithm is based on a neural network trained with simulated  $T_B$  at AMSU frequencies.  $T_B$  are obtained with a two-stream radiative transfer model applied to meteorological fields simulated with a mesoscale numerical weather prediction (NWP) model (MM5), initialized with the National Centres for Environmental Prediction (NCEP) data. Training was made using 122 representative storms covering a wide range of precipitation types between July 2002 and June 2003, selecting only storms for which the maps of simulated brightness temperatures matched simultaneous AMSU observations near  $183 \pm 7$  GHz. The global nature of these storms addresses the principal weakness in statistical methods trained with radar or other non-global data. The validity of these simulated storms is supported by their general agreement with histograms of concurrent AMSU observations.

The algorithm involves a set of signal processing whose outputs are fed into the neural network to produce a rain rate estimate at AMSU-B/MHS grid. The signal processing utilizes techniques such as bilinear interpolation of AMSU-A data to AMSU-B/MHS grid and principal component analysis to identify the signal principal component related to the precipitating cell and to attenuate noises related to surface effects and angle dependence. The algorithm was originally validated by the authors (see Surussavadee and Staelin, 2008b) through numerical comparisons with similar products derived from other systems such as AMSR-E aboard the Aqua satellite, SSM/I aboard the DMSP F-13, F-14 and F-15 satellites, TMI aboard the TRMM satellite and surface precipitation rate product (NOWRAD) using the Next-Generation Weather Radar (NEXRAD) programme.

It should be noted that the Surussavadee and Staelin algorithm has been adopted by us for the EUMETSAT Satellite Application Facility on support to Operational Hydrology and Water Management (H-SAF) – see <http://www.meteoam.it>. Presently, it is under validation within that EUMETSAT programme.

### 3 The Lightning-based Precipitation Evolving Technique (L-PET)

The Surussavadee and Staelin algorithm provides instantaneous precipitation estimates having the same spatial sampling and resolution of AMSU-B/MHS data described in the previous section. In our L-PET, the retrieved rain rates are first re-sampled by linear interpolation in the satellite

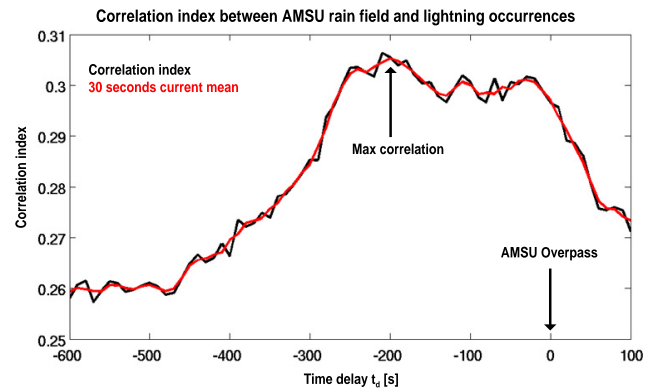


**Fig. 1.** Example of time delay computation for event over center Italy, 1 October 2009 at 13:00 UTC.

cross-track direction to a  $\sim 16$ -km regular grid. Then rain fields are propagated forward in time by means of morphing techniques making use of lightning data organized in a higher-resolution grid. For our applications over the Mediterranean region, we use the lightning data provided by the ZEUS long-range lightning detection network, manufactured by Resolution Displays Inc. This network allows us to retrieve the lightning location with accuracy of 4–5 km (Lagouvardos et al., 2009) by means of the arrival time difference (ATD) triangulation technique. ZEUS' receivers are located at six sites over Europe (in UK, Denmark, Romania, Cyprus, Greece and Portugal) and record the radio noise (sferics) emitted by cloud-to-ground lightning discharges in the very-low-frequency regime (7–15 kHz).

In detail, the working grid is upscaled to 5.33-km resolution grid in order to reduce the beam filling effects due to the satellite 16-km resolution and to take advantage of the higher resolution of the lightning data. To this end, the rain rates are further re-sampled in a new regular grid by dividing each 16-km pixel into  $3 \times 3$  pixels having sizes of 5.33 km. In addition, lightning occurrences are counted for each pixel of the same grid over the adjoining time intervals of width  $\Delta t$  (usually,  $\Delta t = 5$  min) that are centred at time steps  $t'_n = t_0 + n\Delta t + t_d$ , where  $t_0$  is the time of the considered AMSU overpass,  $n = 0, \dots, N$  is the integer that indexes the propagation process and  $t_d$  is the delay between rain field and lightning occurrences (Adamo, 2004). This time lag is introduced in order to synchronize the starting time  $t'_0$  of lightning occurrences with rain field  $\mathbf{RR}_{t_0}$  and it is dynamically computed for each case examined, evaluating the correlation index between  $\mathbf{RR}_{t_0}$  and lightning occurrences matrix in the interval  $t'_0 \pm \Delta t/2$  varying  $t'_0$ . Figure 1 shows an example of this procedure, for the case study occurred on 1 October 2009 over Italy, analysed in Sect. 4. In this case, the correlation between the AMSU rain field  $\mathbf{RR}_{t_0}$  and the lightning occurrence exhibits its maximum value at about  $-200$  s, defining the  $t_d$  used for the whole propagation process.

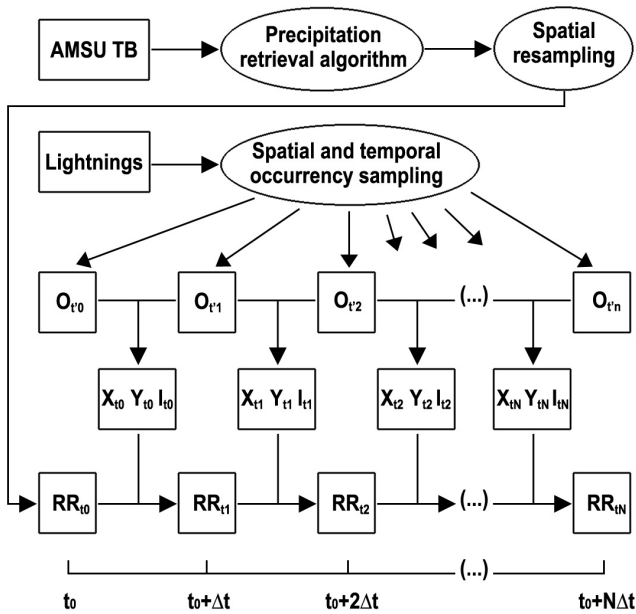


**Fig. 2.** Schematic of the Lightning-based Precipitation Evolving Technique (L-PET).

By so doing, the initial rain rates are organized as one precipitation matrix  $RR_{t_0}$ , the elements of which are the AMSU estimates at  $t = t_0$  for all 5.33-km resolution pixels of the working grid; correspondingly, all lightning measurements are organized as  $N$  occurrences matrices  $O_{t'_n}$  to be used to propagate forward the rain field  $RR_{t_0}$ . Figure 2 provides a schematic representation of the L-PET algorithm. Basically, the technique consists of determining, for each time step  $t_n = t_0 + n\Delta t$ , three matrices to apply to the precipitation matrix  $RR_{t_n}$  in order to build the precipitation matrix  $RR_{t_n+\Delta t}$  for the following time step  $t_{n+1} = t_n + \Delta t$ , i.e., two matrices ( $X_{t_n}$  and  $Y_{t_n}$ ) to identify the horizontal movements in the track and cross-track directions, respectively, and one matrix ( $I_{t_n}$ ) to modulate the rain rates. Note, for each time step  $t_n$ , all these matrices are derived by analysing the lightning occurrences matrices at time steps  $t'_n$  and  $t'_{n+\Delta t}$  ( $O_{t'_n}$  and  $O_{t'_{n+\Delta t}}$ , respectively). Therefore, since the lightning data is acquired in a very short time through the ZEUS network and the time interval  $\Delta t$  is of the order of a few minutes, this procedure effectively allows for real-time monitoring of convective storms.

The first step in determining the  $X_{t_n}, Y_{t_n}$  and  $I_{t_n}$  matrices consists of identifying all sub-matrices  $O_{t'_n}$  of the lightning occurrences matrix  $O_{t'_n}$ , that are defined as the smallest matrices that include the 8-connected regions with lightning within that matrix – where 8-connected regions means that for each pixel (with lightning) of the region, there is at least another pixel (with lightning) of the same region that is vertically or horizontally or diagonally contiguous to the considered one. Thus, we can consider these 8-connected regions as

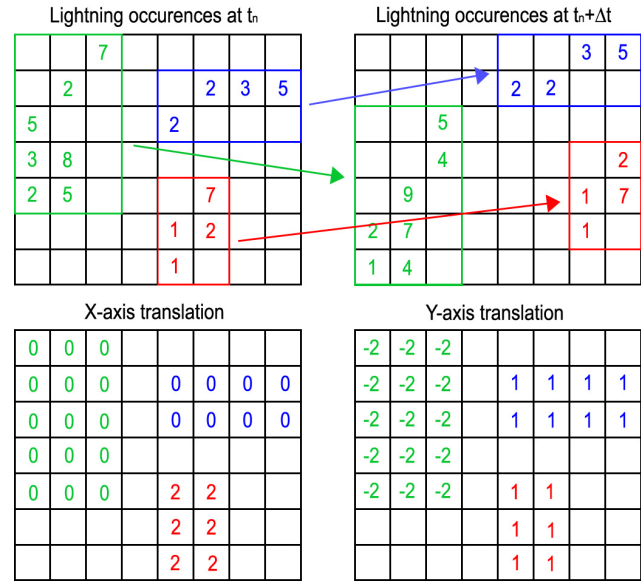


**Fig. 3.** (a and b) Example of lightning occurrence matrix  $O_{t_n}$  and  $O_{t_n+\Delta t}$  showing, in different colours, three different 8-connected cells  $O_{t'_n}$  (a) and the corresponding cells  $s_{t_n+\Delta t}$  (b). The numbers indicate the lightning occurrences in the various 5.33-km resolution pixels of the three cells. (c and d) Corresponding portion of the translation matrix  $X_{t_n}$  and  $Y_{t_n}$  in the cross-track and along-track direction, respectively.

representative of different convective cells (or multicell systems) and the aim is to follow their evolution in time and space. Figure 3a shows an example of this identification procedure. Here, the lightning occurrences matrix  $O_{t'_n}$  contains three different 8-connected regions (i.e., three different convective cells, or multicell systems) that are identified by three different colours; for each region, the same colour is used both for the number of lightning occurrences in each of the 5.33-km resolution pixels of the cell and for marking the borders of the corresponding sub-matrix  $O_{t'_n}$ .

The second step consists of identifying the translational movements of the various cells. This is accomplished by first evaluating the correlation indices of each sub-matrix  $O_{t'_n}$  with all sub-matrices  $O_{t'_{n+\Delta t}}$  of matrix  $O_{t'_{n+\Delta t}}$  that are within 4 pixels (i.e., within  $\sim 16$  km) along the track and cross-track directions – a requirement necessary to limit ambiguities in detecting cell movements (the 4-pixel value corresponds to an upper limit of about  $130 \text{ km h}^{-1}$  for the velocity of the convective cells). Then, the translational movement having the maximum correlation index is chosen and the components of the selected displacement are stored in matrices  $X_{t_n}$  and  $Y_{t_n}$  (see Fig. 3c and d). Note, since at this stage only the shape of the cells is considered, the correlation is computed using the binary versions of  $O_{t'_n}$  and  $O_{t'_{n+\Delta t}}$ , that are obtained by assigning 0/1 to the various 5.33-km pixels depending on the absence/presence of lightning strokes.

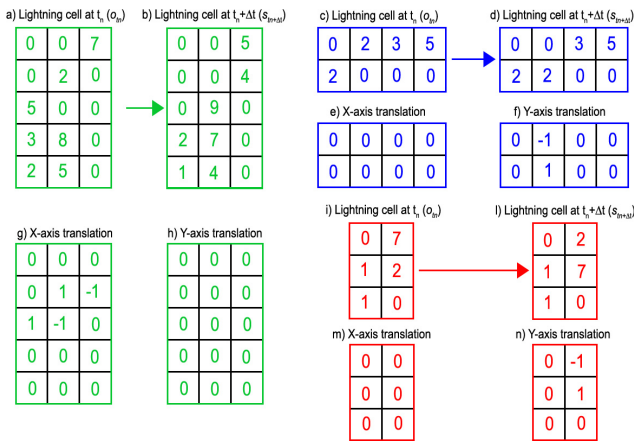


**Fig. 4.** Example of pixel scrambling for three lightning cell: 8-connected cells  $\mathbf{O}_{t_n}$  of  $\mathbf{O}_{t_n}$  at time  $t = t_n$  (panels a, c and i), relative matrices  $s_{t_n+\Delta t}$  of  $\mathbf{O}_{t_n+\Delta t}$  at time  $t = t_n + \Delta t$  (panels b, d and l), and corresponding  $\mathbf{X}_{t_n}$  and  $\mathbf{Y}_{t_n}$  translation in the cross-track and along-track direction, respectively (panels e–f, g–h and m–n).

Defining  $s_{t_n+\Delta t}$  the sub-matrix of  $\mathbf{O}_{t_n+\Delta t}$  corresponding to the position of the cell  $\mathbf{O}_{t_n}$  after the previous step, in the third step, to each cell  $\mathbf{O}_{t_n}$  is applied a pixels scrambling and/or a shape morphing procedure in order to obtain a new cell  $m_{t_n}$  (that we call “morphed”), having the same total lightning occurrences of the  $\mathbf{O}_{t_n}$ , but having maximized the correlation with matrix  $s_{t_n+\Delta t}$ . This operation over  $\mathbf{O}_{t_n}$  is described by two further movement matrices whose values will be added to  $\mathbf{X}_{t_n}$  and  $\mathbf{Y}_{t_n}$ . In case of different pixel scramblings generating the same maximum correlation index, again the smallest movement is preferred (see Fig. 4).

As for  $\mathbf{X}_{t_n}$  and  $\mathbf{Y}_{t_n}$  matrices, also the modulation matrix  $\mathbf{I}_{t_n}$  will be the composite of cell-by-cell sub-matrices, each one obtained by computing the ratio of  $m_{t_n}$  and  $s_{t_n+\Delta t}$  and averaging the result on the box  $(3 \times 3)$ . Finally, to avoid instability, the elements of the above matrix are limited in the empirical interval  $(0.5–1.5)$  to generate the final matrix  $\mathbf{I}_{t_n}$  that will be applied to  $\mathbf{RR}_{t_n+\Delta t}$  in order to modulate the intensity of precipitation according to the increase or decrease of the lightning strokes frequency.

At this stage not all of the elements of the matrices  $\mathbf{X}_{t_n}$ ,  $\mathbf{Y}_{t_n}$  and  $\mathbf{I}_{t_n}$  are defined because there are regions without lightning. To complete the matrices, each not defined element is filled with the average of the contiguous defined elements, iterating until each element is defined.

This treatment is necessary to propagate the information provided by lightning to the whole rain field, covering also the precipitative regions without registered electrical activity.

As depicted in Fig. 2, the movements matrices  $\mathbf{X}_{t_n}$ ,  $\mathbf{Y}_{t_n}$  and the modulation matrix  $\mathbf{I}_{t_n}$  are applied to the rain rate matrix  $\mathbf{RR}_{t_n}$ , creating in this way the morphed matrix  $\mathbf{RR}_{t_n+\Delta t}$ , that is the new rain field to propagate in the next iteration.

However, the algorithm also includes a part necessary to take into account for the generation of new precipitation

cells. As a matter of fact, working on  $\mathbf{I}_{t_n}$  allows the increase or decrease of the precipitation of an existing cell, including the eventual complete extinction of the cell, but the formation of new cells is not possible since the modulation of  $\mathbf{RR}_{t_n}$  for each pixel without precipitation is always null because the  $\mathbf{I}_{t_n}$  is applied to  $\mathbf{RR}_{t_n}$  by means of a simple multiplication.

To solve this problem, we define  $M_{t_n}$  as the averaged precipitation corresponding to one lightning stroke, that is computed as the ratio between the total precipitation and the total number of lightning strokes occurred in the whole area under examination. This value  $M_{t_n}$  is then used as a factor to multiply the averaged lightning strokes occurring in each box  $(3 \times 3)$  around pixels having no precipitation in  $\mathbf{RR}_{t_n+\Delta t}$  matrix. In so doing, new precipitative cells will appear where new lightning cells are detected.

Finally, the propagated precipitation field is averaged over box  $(3 \times 3)$  and resampled to 16 km resolution in order to obtain the same resolution of the original AMSU-based precipitation estimate.

#### 4 Analysis of 1 October 2009 case study over Sicily

On 30 September 2009, a depression developed over Northern Africa with a warm advection from the Sahara to the Mediterranean region, culminating in an extraordinary intense rainfall from 12:00 to 20:00 UTC on 1 October 2009. The heavy rainfall had discharged an amount of more than 200 mm in southern Italy, near the island of Sicily. Figure 5, left panel, shows a map of mean sea level pressure and 500 hPa geopotential at 00:00 UTC on 1 October, in which there was a low over Algeria corresponding to a southern flux at a non-divergent level. Figure 5, right panel, shows a map of winds and thermal field at 850 mbar level, which points out the strong warm advection over Northern Africa. The interaction with the complex topography generated gravity waves and convergence lines that triggered extensive and strong convection over the sea with the dispersal of moisture throughout Italy. During the day of 1 October, the cyclone deepened and it moved east creating a sustained condition of bad weather over Sicily with heavy convective rainfall that provoked a large landslide near Messina, claiming two victims.

Figure 6 shows the evolution of the precipitation every 15 min on a 16 km regular grid, from 13:00 UTC to 15:45 UTC, as estimated by the L-PET algorithm with  $\Delta t$  equal to 5 min, starting from the rain field provided by the AMSU-based algorithm at 13:00 UTC. In each panel, as reference, the lightning occurrences matrix  $\mathbf{O}_{t_n}$  on 5.33 km regular grid has also been included.

The first panel, corresponding to 13:00 UTC, shows an overall correlation between the pattern of precipitation, as provided by the AMSU-based algorithm, and the position of lightning occurrences. Pattern similarities are more evident where higher precipitations are estimated, such as over

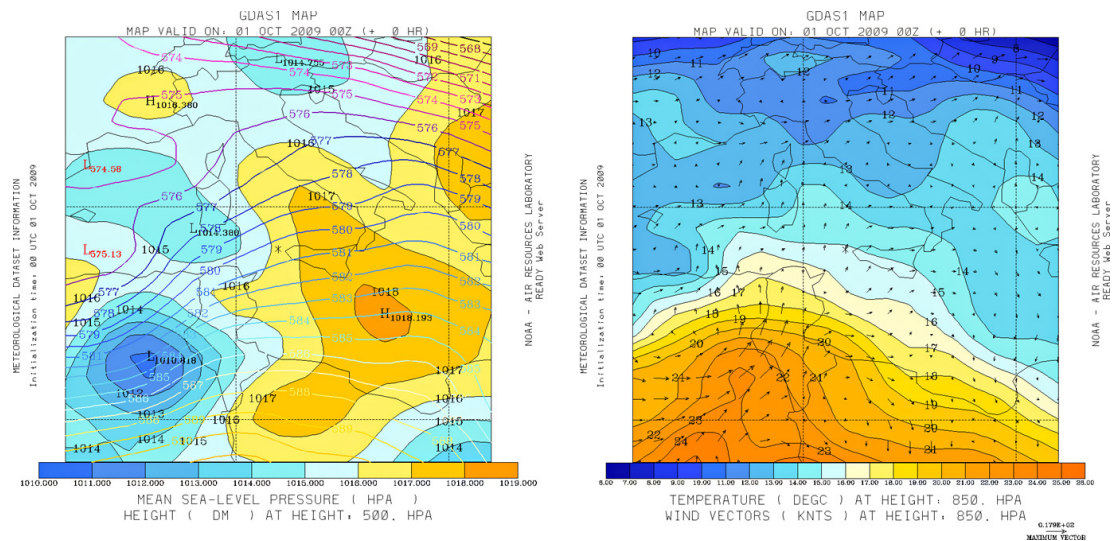


**Fig. 5.** National Centres for Environmental Prediction (NCEP) Global Data Assimilation System (GDAS) model output on 00:00 UTC of 1 October 2009 – Left panel) Mean sea level pressure and 500 mbar level geopotential – Right panel) Winds and thermal field at 850 mbar level.

the Strait of Sicily. The correlation decreases with decreasing precipitation intensity and lightning occurrences, such as over Tunisia and over eastern Sicily or Sardinia. The good correlation between large lightning occurrences and heavy precipitating storms is a well-recognized consequence of the fact that the generation of charged clouds is due to intense convection coupled with the updraft of graupel and ice particles (i.e., Solomon et al., 2005). The following lightning discharge and following precipitation have temporal and/or spatial displacement depending on the dynamical characteristics of the storm. Fixed  $t_d$  by using the procedure in Fig. 1, now in Fig. 6 we recognize that precipitation and lightning are spatially correlated. For our purposes, this is enough to hook precipitation to lightning and propagate the rain field using lightning until a new estimation of precipitation from one LEO satellite will update our storm view. Unfortunately, we have few lightning strokes in some regions of Fig. 6 that mainly correspond to a lower precipitation part of the storm. It makes the reconstruction of the whole rain field objectively less accurate. In addition, the situation is further complicated due to the fact that MW remote-sensing is more efficient in observing high precipitation (Bennartz et al., 2006). This explains the low correlation observed between low precipitation and low lightning occurrences.

In the following 5 panels of Fig. 6, between 13:15 UTC and 14:15 UTC, it is possible to observe that the most intense lightning cell tends to stretch and move south while the lightning occurrences to the north of Sicily, over the Tyrrhenian Sea and Sardinia, tend to decrease. The L-PET algorithm correctly follows this development, stretching and shifting to Tunisia the most intense precipitation cell and decreasing the precipitation area over the Tyrrhenian Sea, separating it from

the main cell and decreasing it in extension and in intensity until it disappears completely in the following panels. It is interesting to observe that the L-PET algorithm restructures the shape of the low precipitation cell over Sardinia, remodulating it along corresponding lightning occurrence cells. Also, the weak precipitation cell over Eastern Sicily at 13:00 UTC follows the lightning evolution, falling rapidly and disappearing altogether at 13:30 UTC. The small precipitation that appears over Calabria at 14:00 UTC, associated with very weak lightning occurrence, is an example of the L-PET algorithm's capability to generate new cells in case lightning appears in areas without precipitation.

In the last 6 panels of Fig. 6, between 14:30 UTC and 15:45 UTC, one can observe a progressive movement eastward of the main lightning occurrence cell as it splits into two cells, the largest over the Strait of Sicily and the smaller one over Northern Sicily. This lightning activity intensification near Sicily is accompanied by the gradual disappearance of sporadic lightning over Sardinia and the Tyrrhenian Sea. This evolution of lightning field is followed by the L-PET algorithm with equivalent changes in the rain field, with the formation of two high precipitation cells and the end of the low precipitation areas over Sardinia and the Tyrrhenian Sea. Note also a new weak precipitation cell over eastern Sicily corresponding to sporadic lightning occurrence in the Strait of Messina.

## 5 Evaluation of performances

Generally, the comparison with available radars or rain gauge measurements represents a good reference to understand the reliability of rain fields estimated by satellite-based

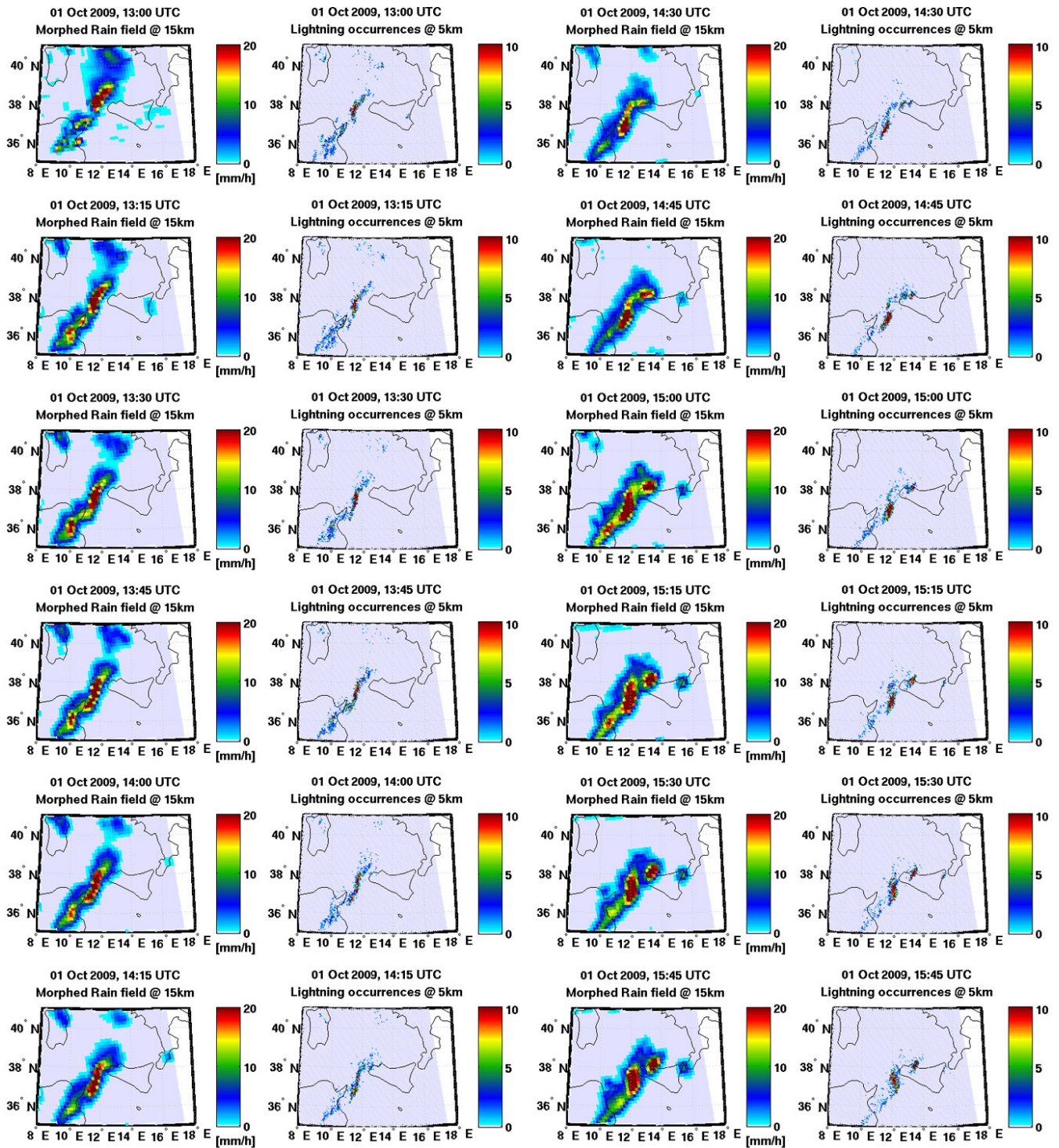


**Fig. 6.** Event over southern Italy, 1 October 2009. L-PET estimated rain field evolution from 13:00 UTC to 15:45 UTC, starting from the rain field provided by the AMSU-based algorithm applied to TB from NOAA 18 satellite, and contemporary lightning occurrences used for the algorithm.

instruments. In this paper, the focus is on the evaluation of the L-PET algorithm in reproducing the AMSU estimates when AMSU instruments are not passing over the region. So that, to exclude the uncertainties related to the performance

of the AMSU-based retrieval algorithm from the evaluation of the results, it is more interesting to compare the performance of the L-PET versus the next AMSU-based retrieved rain field following the first one. This comparison is shown

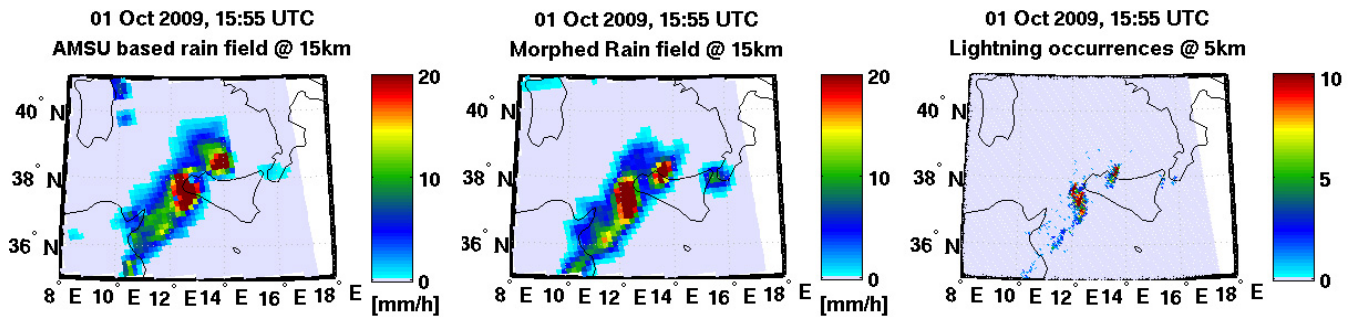


**Fig. 7.** Rain field provided by the AMSU-based algorithm applied to TB from NOAA 15 satellite compared with contemporary rain field provided by L-PET algorithm and lightning occurrences used for the algorithm, over southern Italy region, 1 October 2009 at 15:55 UTC.

in Fig. 7, where the rain field propagated from 13:00 UTC to 15:55 UTC is compared with the new satellite-based rain field at 15:55 UTC.

Although the precipitation values pixel-by-pixel are different in the two panels, the maps describe a quite similar precipitating pattern and similar values, showing an overall reliability of this technique. The most interesting result shown in Fig. 7 is the correct identification of the two most intense cells, at  $\sim 20 \text{ mm h}^{-1}$ , and the tail of the main precipitation cell, at  $\sim 10 \text{ mm h}^{-1}$ , near the coast of Tunisia, especially for distributions of precipitation intensity values. In this case, we note that the estimates of the whole precipitation area by the L-PET algorithm are a bit shifted, if compared with those derived from AMSU, by about 15 km to the east and 30 km to the south. Looking at the third panel of the same figure, it is clear that this shift is a direct consequence of lightning positions in respect to the most intense precipitation region in the AMSU-based rain field estimates. Another problem that emerges in observing Fig. 7 is that few low precipitation areas are not correctly reproduced, such as over Northern Sardinia in which the precipitation pattern is not well identified, or over the Strait of Messina in which the pattern is a bit too large and the value a bit too intense. Observing the third panel in Fig. 7, it is clear that there is very low lightning occurrences in these two regions and consequently it is reasonable that the algorithm cannot provide good rain field estimates. Figure 8 describes the statistics of rain fields shown in Fig. 7 using histograms, maximum value, mean and standard deviation of rain rate (RR), evidencing an overall agreement.

It is interesting to test the L-PET when applied to a completely different precipitation case. Figures 9 and 10 show results for an intense rainfall occurred in central Europe on 15 July 2009. In this case, due to the large gap between two consecutive AMSU-equipped satellite overpasses, the L-PET rainfall propagation has been used to cover about 5 hours of the evolution of the rain field (from 15:28 to 20:08 UTC). Even if the latitude and the season of this case study is different, and it is over land, the performances appear very similar.

However, there are some differences from L-PET and AMSU-based rain field. Even if part of those differences

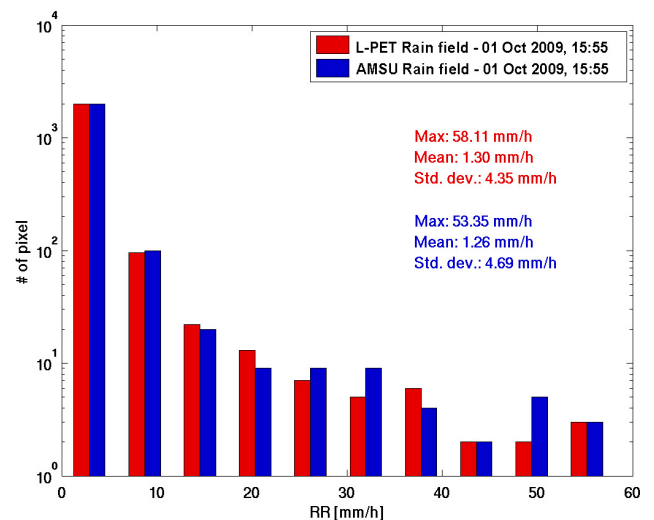


**Fig. 8.** Statistics of rain field provided by the AMSU-based algorithm applied to TB from NOAA 15 satellite (blue) and rain field provided by L-PET algorithm (red), over southern Italy region, 1 October 2009 at 15:55 UTC.

is probably due to the L-PET, it should be noted that the two rain fields of the case study occurred over Sicily at 13:00 UTC and 15:55 UTC, are estimated from two different satellites, respectively NOAA 18 and NOAA 15, which have the high frequency MW instruments (AMSU-B and MHS) slightly different. In addition, the NOAA 15 AMSU-B channels are significantly asymmetric and suffer from radio frequency interference (Buehler et al., 2005) that reduces the quality of the rain field retrieved. Also for the case study occurred over Central Europe at 15:28 UTC and 20:08 UTC, we have two different satellites, respectively NOAA 15 and MetOP-A, and then the high frequency MW instruments (AMSU-B and MHS) are also slightly different, in addition to the same problem for NOAA 15 AMSU-B channels.

Despite these conditions, we consider the agreement between AMSU-based rain field and L-PET rain field satisfactory.

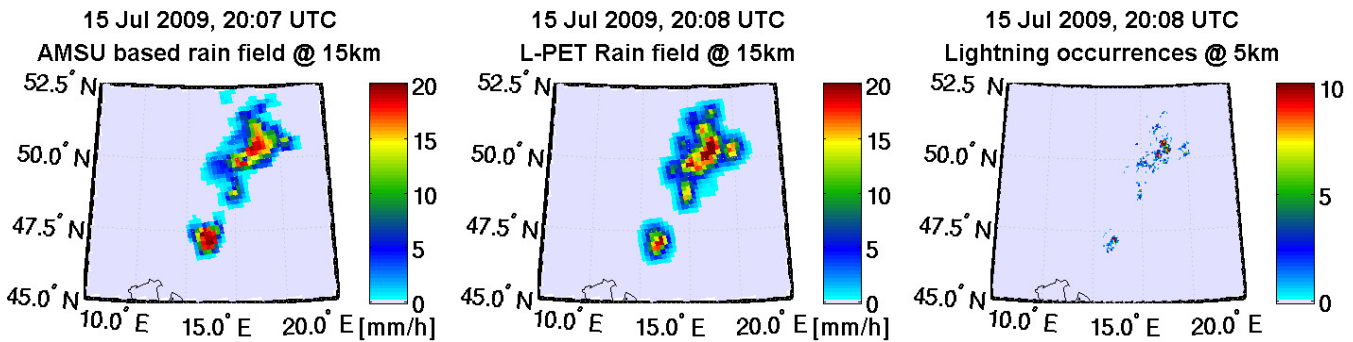


**Fig. 9.** Rain field provided by the AMSU-based algorithm applied to TB from MetOp-A satellite compared with contemporary rain field provided by L-PET algorithm and lightning occurrences used for the algorithm, over central Europe, 15 July 2009 at 20:07 UTC.

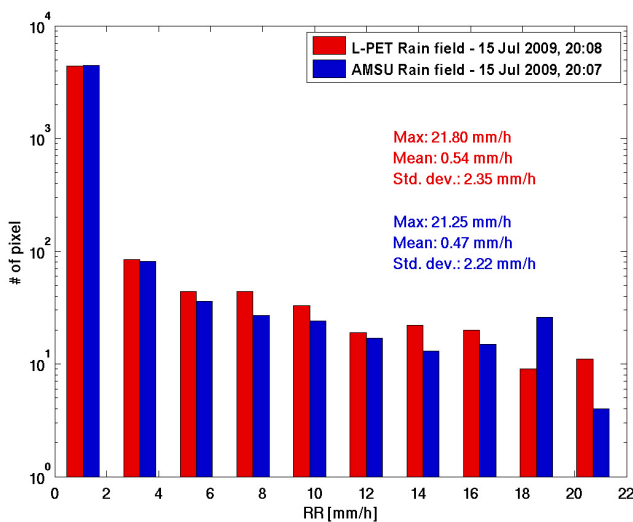


**Fig. 10.** Statistics of rain field provided by the AMSU-based algorithm applied to TB from MetOp-A satellite (blue) and rain field provided by L-PET algorithm (red), over central Europe, 15 July 2009 at 20:07 UTC.

## 6 Conclusions

The examples we have shown in the previous sections are typical cases in which the frequency of satellite overpass is not sufficient to give an adequate passive MW temporal coverage of the event. Quickly evolving precipitation cells, often embedded in wider storm systems, are generally hidden by the wide area saturation of the IR measurements and often also misplaced because parallax problems occur when geostationary instruments are used. The L-PET has been developed expressly to give continuity to the observation of precipitative regimes for these kinds of cases, which are very common over the Mediterranean regions, especially where complex orography and coastal effects very often break into fragments of organized advecting storm systems during summer and early autumn months.

A further quantitative analysis of the method will be carried out by the authors, analysing more case studies in order to optimize some technical choices such as  $\Delta t$ ,  $t_d$  and the allowed upper limit velocity for the convective cells. In addition, future works include also a wider calibration/validation of the method. Nevertheless, the capability of the L-PET to hook the evolution of the pattern has been shown in this work, and it is an evident characteristic worthy of being exploited in satellite-based monitoring. Obviously this technique works if there is a meaningful presence of lightning and it depends both on the type of the storm and on the sensitivity of the lightning network. To overcome this problem, we plan to also include IR data in the future release of L-PET propagation strategy.

AMSU and ZEUS data are available in quasi-real-time, so an operational tool based on L-PET strategy can represent a new source of information for meteorologists, forecasters and other people interested in mitigating catastrophes caused by heavy rain events.

*Acknowledgements.* This research has been supported by the European Commission Sixth Framework Programme through the project “Observation, Analysis and Modelling of Lightning Activity in Thunderstorms, for use in Short Term Forecasting of Flash Floods” (FLASH), by the European Community Initiative INTERREG III-B ARCHIMED through the project “Weather Risk Reduction in the Central and Eastern Mediterranean” (RISKMED), and by the Italian FISR-MIUR programme “Sustainable Development and Climate Changes” through the project “Aerosol Effects on Clouds and Climate” (AEROCLOUDS). It is also included in the research activities of Satellite Application Facility on Support to Operational Hydrology and Water Management (H-SAF) funded by EUMETSAT and supported by the Italian Civil Protection Department.

Edited by: G. Boni

Reviewed by: T. Rigo, C. Price, and another anonymous referee

## References

- Adamo, C.: On the use of lightning measurements for the microphysical analysis and characterization of intense precipitation events over the Mediterranean area, PhD Thesis, University of Ferrara, Italy, 2004.
- Adamo, C., Solomon, R., Medaglia, C. M., Dietrich, S., and Mugnai, A.: Cloud microphysical properties from remote sensing of lightning within the Mediterranean, in: *Measuring Precipitation from Space – EURAINSAT and the Future*, edited by: Levizzani, V., Bauer, P., and Turk, F. J., Springer, 127–134, 2007.
- Adamo, C., Goodman, S., Mugnai, A., and Weinman, J. A.: Lightning measurements from satellites and significance for storms in the Mediterranean, in: *Lightning: Principles, Instruments and Applications*, edited by: Betz, H.-D., Schumann, U., and Laroche, P., Springer, 309–329, 2009.
- Adler, R. F., Huffman, G. J., and Keehn, P. R.: Global tropical rain estimates from microwave-adjusted geosynchronous IR data, *Remote Sens. Rev.*, 11, 125–152, 1994.
- Bennartz, R., Thoss, A., Dybbroe, A., and Michelson, D. B.: Precipitation analysis using the Advanced Microwave Sounding Unit in support of Nowcasting applications, *Meteorol. Appl.*, 9(2), 177–189, 2006
- Betz, H.-D., Schmidt, K., Oettinger, W. P., and Montag, B.: Cell-tracking with lightning data from LINET, *Adv. Geosci.*, 17, 55–61, 2008, <http://www.adv-geosci.net/17/55/2008/>.
- Bizzarri, B., Di Paola, F., and Dietrich, S.: Resolution enhancement of millimetre-submillimetre wave images from geostationsry orbit, Final Report, EUMETSAT contract EUM/CO/04/1386/KJG “Simulations and User Requirements Review for Precipitating Clouds from Geostationary Orbits in mm/sub-mm Bands”, 94 pp., 2005.
- Bizzarri, B., Gasiewski, A. J., and Staelin, D. H.: Observing rain by millimetre-submillimetre wave sounding from geostationary orbit, in: *Measuring Precipitation from Space – EURAINSAT and the Future*, edited by: Levizzani, V., Bauer, P., and Turk, F. J., Springer, 675–692, 2007.
- Bonelli, P. and Marcacci, P.: Thunderstorm nowcasting by means of lightning and radar data: algorithms and applications in northern Italy, *Nat. Hazards Earth Syst. Sci.*, 8, 1187–1198, doi:10.5194/nhess-8-1187-2008, 2008.
- Buehler, S. A., Kuvatov, M., and John, V. O.: Scan asymmetries in AMSU-B data, *Geophys. Res. Lett.*, 32, L24810, doi:10.1029/2005GL024747, 2005.
- Di Paola, F., and Dietrich, S.: Resolution enhancement for microwave-based atmospheric sounding from geostationary orbits, *Radio Sci.*, 43, RS6001, doi:10.1029/2007RS003789, 2008.
- Ebert, E. E., Janowiak, J. E., and Kidd, C.: Comparison of near-real-time precipitation estimates from satellite observations and numerical models, *Bull. Amer. Meteor. Soc.*, 88, 47–64, 2007.
- Gasiewski, A. J.: Numerical sensitivity analysis of passive EHF and SMMW channels to tropospheric water vapor, clouds and precipitation, *IEEE Trans. Geosci. Remote Sens.*, 30, 859–870, 1992.
- Huffman, G. J., Adler, R. F., Curtis, S., Bolvin, D. T., and Nelkin, E. J.: Global rainfall analyses at monthly and 3-h time scales, in: *Measuring Precipitation from Space – EURAINSAT and the Future*, edited by: Levizzani, V., Bauer, P., and Turk, F. J., Springer, 291–305, 2007.
- Joyce, R. J., Janowiak, J. E., Arkin, P. A., and Xie, P.: CMORPH: a method that produces global precipitation estimates from passive microwave and infrared data at high spatial and temporal resolution, *J. Hydromet.*, 5, 487–503, 2004.
- Joyce, R. J., Janowiak, J. E., Xie, P., and Arkin, P. A.: CPC MORPHING technique (CMORPH), in: *Measuring Precipitation from Space – EURAINSAT and the Future*, edited by: Levizzani, V., Bauer, P., and Turk, F. J., Springer, 307–317, 2007.
- Kidd, C., Kniveton, D. R., Todd, M. C., and Bellerby, T. J.: Satellite rainfall estimation using combined passive microwave and infrared algorithms, *J. Hydromet.*, 4, 1088–1104, 2003.
- Kidd, C., Tapiador, F. J., Sanderson, V., and Kniveton, D.: The University of Birmingham global rainfall algorithms, in: *Measuring Precipitation from Space – EURAINSAT and the Future*, edited by: Levizzani, V., Bauer, P., and Turk, F. J., Springer, 255–267, 2007.
- Kotroni, V. and Lagouvardos, K.: Lightning occurrence in relation with elevation, terrain slope and vegetation cover in the Mediterranean, *J. Geophys. Res.*, 113, D21118, doi:10.1029/2008JD010605, 2008.
- Kramer, H. J.: *Observation of the Earth and Its Environment*, Springer-Verlag, 1510 pp., 2002.
- Kubota, T., Shige, S., Hashizume, H., Aonashi, K., Takahashi, N., Seto, S., Hirose, M., Takayabu, Y. N., Nakagawa, K., Iwanami, K., Ushio, T., Kachi, M., and Okamoto, K.: Global precipitation map using satelliteborne microwave radiometers by the GSMaP project: production and validation, *IEEE Trans. Geosci. Remote Sens.*, 45, 2259–2275, 2007.
- Lagouvardos, K., Kotroni, V., Betz, H.-D., and Schmidt, K.: A comparison of lightning data provided by ZEUS and LINET networks over Western Europe, *Nat. Hazards Earth Syst. Sci.*, 9, 1713–1717, doi:10.5194/nhess-9-1713-2009, 2009.
- Llasat, M. C., Llasat-Botija, M., Prat, M. A., Porcú, F., Price, C., Mugnai, A., Lagouvardos, K., Kotroni, V., Katsanos, D., Michaelides, S., Yair, Y., Savvidou, K., and Nicolaides, K.: High-impact floods and flash floods in Mediterranean countries: the FLASH preliminary database, *Adv. Geosci.*, 23, 47–55, 2010, <http://www.adv-geosci.net/23/47/2010/>.
- Mugnai, A. and Pinori, S.: Precipitation retrieval from GEO by millimeter-submillimetre wave radiometry, Final Report, EUMETSAT contract EUM/CO/04/1386/KJG “Simulations and User Requirements Review for Precipitating Clouds from Geostationary Orbits in mm/sub-mm Bands”, 45 pp., 2005.
- Petersen, W. A. and Rutledge, S. A.: On the relationship between cloud-to-ground lightning and convective rainfall, *J. Geophys. Res.*, 103(D12), 14025–14040 1998.
- Pieppgrass, M. V. and Krider, E. P.: Lightning and surface rainfall during Florida thunderstorms, *J. Geophys. Res.*, 87, 11193–11201, 1982.
- Rivas Soriano, L., de Pablo, F., and Garcia Diez, E.: Relationship between convective precipitation and cloud-to-ground lightning in the Iberian Peninsula, *Mon. Weather Rev.*, 129, 2998–3003, 2001.
- Sheridan, S. C., Griffiths, J. F., and Orville, R. E.: Warm season cloud-to-ground lightning – precipitation relationships in the south-central United States, *Wea. Forecasting*, 12, 449–458, 1997.
- Smith, E. A., Asrar, G., Furuhashi, Y., Ginati, A., Mugnai, A., Nakamura, K., Adler, R. F., Chou, M.-D., Debois, Durning, J.

- F., Entin, J. K., Einaudi, F., Ferraro, R. R., Guzzi, R., Houser, P. R., Hwang, P. H., Iguchi, Joe, P., T., Kakar, R., Kaye, J. A., Kojima, M., Kummerow, C., Kuo, K.-S., Lettenmaier, D. P., Levizzani, V., Lu, N., Mehta, A. V., Morales, C., Morel, P., Nakazawa, T., Neeck, S. P., Okamoto, K., Oki, R., Raju, G., Shepherd, J. M., Simpson, J., Sohn, B.-J., Stocker, E. F., Tao, W.-K., Testud, J., Tripoli, G. J., Wood, E. F., Yang, S., and Zhang, W.: International Global Precipitation Measurement (GPM) program and mission: an overview, in: *Measuring Precipitation from Space - EURAINSAT and the Future*, edited by: Levizzani, V., Bauer, P., and Turk, F. J., Springer, 611–653, 2007.
- Solomon, R., Medaglia, C. M., Adamo, C., Dietrich, S., Mugnai, A., Biader, U.: An Explicit Microphysics Thunderstorm Model, *International Journal of Modelling and Simulation*. 25(2), 112–118, 2005.
- Soula, S., Sauvageot, H., Molinié, G., Mesnard, F., and Chauzy, S.: The CG lightning activity of storm causing a flashflood, *Geophys. Res. Lett.*, 25(8), 1181–1184, 1998.
- Surussavadee, C. and Staelin, D. H.: Global millimeter-wave precipitation retrievals trained with a cloud-resolving numerical weather prediction model, Part I: Retrieval design, *IEEE Trans. Geosci. Remote Sens.*, 46, 99–108, 2008a.
- Surussavadee, C. and Staelin, D. H.: Global millimeter-wave precipitation retrievals trained with a cloud-resolving numerical weather prediction model, Part II: Performance evaluation, *IEEE Trans. Geosci. Remote Sens.*, 46, 109–118, 2008b.
- Tapia, T., Smith, J. A., and Dixon, M.: Estimation of convective rainfall from lightning observations, *J. Appl. Meteor.*, 37, 1497–1509, 1998.
- Torricella, F., Levizzani, V., and Turk, F. J.: Application of a blended MW-IR rainfall algorithm to the Mediterranean, in: *Measuring Precipitation from Space – EURAINSAT and the Future*, edited by: Levizzani, V., Bauer, P., and Turk, F. J., Springer, 497–507, 2007.
- Turk, F. J., Rohaly, G. D., Hawkins, J., Smith, E. A., Marzano, F. S., Mugnai, A., and Levizzani, V.: Meteorological applications of precipitation estimation from combined SSM/I, TRMM and infrared geostationary satellite data, in: *Microwave Radiometry and Remote Sensing of the Earth's Surface and Atmosphere*, edited by: Pampaloni, P., and Paloscia, S., VSP Press, 353–363, 2000.
- Turk, F. J. and Mehta, A. V.: Towards improvements in short-time scale satellite-derived precipitation estimates using blended satellite techniques, in: *Measuring Precipitation from Space – EURAINSAT and the Future*, edited by: Levizzani, V., Bauer, P., and Turk, F. J., Springer, 281–290, 2007.